



Dynamics of SLC25A51 reveal preference for oxidized NAD⁺ and substrate led transport

Shivansh Goyal¹ , Akhilesh Paspureddi² , Mu-Jie Lu¹ , Hsin-Ru Chan¹, Scott N Lyons¹, Crystal N Wilson¹, Marc Niere³ , Mathias Ziegler³  & Xiaolu A Cambronne^{1,4,*} 

Abstract

SLC25A51 is a member of the mitochondrial carrier family (MCF) but lacks key residues that contribute to the mechanism of other nucleotide MCF transporters. Thus, how SLC25A51 transports NAD⁺ across the inner mitochondrial membrane remains unclear. To elucidate its mechanism, we use Molecular Dynamics simulations to reconstitute SLC25A51 homology models into lipid bilayers and to generate hypotheses to test. We observe spontaneous binding of cardiolipin phospholipids to three distinct sites on the exterior of SLC25A51's central pore and find that mutation of these sites impairs cardiolipin binding and transporter activity. We also observe that stable formation of the required matrix gate is controlled by a single salt bridge. We identify binding sites in SLC25A51 for NAD⁺ and show that its selectivity for NAD⁺ is guided by an electrostatic interaction between the charged nicotinamide ring in the ligand and a negatively charged patch in the pore. In turn, interaction of NAD⁺ with interior residue E132 guides the ligand to dynamically engage and weaken the salt bridge gate, representing a ligand-induced initiation of transport.

Keywords MCART1; mitochondrial carrier family; mitochondrial transport; nicotinamide adenine dinucleotide (NAD); SLC25A51

Subject Categories Membranes & Trafficking; Metabolism; Organelles

DOI 10.15252/embr.202256596 | Received 1 December 2022 | Revised 23 July 2023 | Accepted 27 July 2023 | Published online 14 August 2023

EMBO Reports (2023) 24: e56596

Introduction

SLC25A51 is an essential gene that is ubiquitously expressed across all mammalian cells. Its protein controls the concentration of NAD⁺ in the mitochondrial matrix by directly importing the oxidized dinucleotide, and thus, mammalian mitochondria depend on SLC25A51 for sustaining NAD⁺ levels (Girardi *et al.*, 2020; Kory *et al.*, 2020; Luongo *et al.*, 2020). Loss of SLC25A51 resulted in loss of cellular respiration and oxidative flux of the tricarboxylic acid cycle. SLC25A51 further impacted the concentrations of

NAD-derived metabolites and cofactors, including NADH and NADPH (Girardi *et al.*, 2020; Kory *et al.*, 2020; Luongo *et al.*, 2020).

There is little understood, nevertheless, about the underlying mechanisms of SLC25A51 or how the transporter interacts with oxidized NAD⁺. SLC25A51 is a member of the mitochondrial carrier family (MCF) that localizes to the inner mitochondrial membrane (Girardi *et al.*, 2020; Kory *et al.*, 2020; Luongo *et al.*, 2020; Ziegler *et al.*, 2021). By homology, its structure harbors a pseudo-tri-symmetrical pore that is characteristic of the family (Pebay-Peyroula *et al.*, 2003; Robinson *et al.*, 2008; Ruprecht & Kunji, 2021; Ziegler *et al.*, 2021; Jones *et al.*, 2023; Kang & Chen, 2023). The trice repeated domain comprises two transmembrane helices joined by a short matrix helix parallel to the membrane. Based on cytoplasmic and matrix-open structures of the related ADP/ATP nucleotide carriers, it is surmised that members of this structurally related family function through an alternating-access mechanism (Pebay-Peyroula *et al.*, 2003; Nury *et al.*, 2005; Robinson *et al.*, 2008; Ruprecht *et al.*, 2014; King *et al.*, 2016; Springett *et al.*, 2017; Ruprecht & Kunji, 2021).

SLC25A51 has low conservation (< 20%) in its amino acid sequence compared to its functional homologs in *S. cerevisiae* and *A. thaliana* that selectively import mitochondrial NAD⁺ (Fig EV1) (Todisco *et al.*, 2006; Palmieri *et al.*, 2009; Ziegler *et al.*, 2021). In phylogenetic analyses, SLC25A51 did not cluster with other mammalian nucleotide carriers in the family (Robinson *et al.*, 2008; Palmieri, 2013). Thus, it remains unanswered how SLC25A51 engages and transports its ligand.

In this work, we used Molecular Dynamics (MD) simulations to study how SLC25A51 homology models engage the NAD⁺ ligand under the constraints of thermodynamics and in the context of a lipid environment. We tested our observations in intact cells with mutational analysis, measurements of *in situ* free mitochondrial NAD⁺ concentrations using a LigA-based NAD⁺ biosensor (Cambronne *et al.*, 2016) and developed a heterologous uptake system to monitor SLC25A51 activity in recombinant *E. coli* membranes. This study provides the first insight into the binding site of an NAD⁺ mitochondrial transporter, identifies a mechanism of ligand-induced transport, and reveals cardiolipin-binding as a regulator of SLC25A51 activity and consequently mitochondrial NAD⁺ concentrations.

¹ Department of Molecular Biosciences, University of Texas at Austin, Austin, TX, USA

² Department of Chemical Engineering, University of Texas at Austin, Austin, TX, USA

³ Department of Biomedicine, University of Bergen, Bergen, Norway

⁴ Livestrong Cancer Institute, University of Texas at Austin, Austin, TX, USA

*Corresponding author. Tel: +1 512-232-1928; E-mail: lulu@austin.utexas.edu

Results and Discussion

Stable modeling of SLC25A51 in a lipid bilayer

To study how SLC25A51 recognizes NAD^+ , we first generated apo models of human SLC25A51 in its outward-facing, cytoplasmic (c-state) conformation using Swiss-Model and AlphaFold2 modeling (Waterhouse *et al*, 2018; Jumper *et al*, 2021). Both model structures adopted the characteristic MCF fold and were superimposable upon the solved bovine ANT crystal structure (PDB ID: 1OKC) (Pebay-Peyroula *et al*, 2003). Using MolProbity, we determined that the quality of the equilibrated AlphaFold2 and Swiss-Model structures were in the 100th and 97th percentile, respectively (Williams *et al*, 2018). Model quality was further estimated using pLDDT for AlphaFold2 (Fig EV2A) and QMEANDisCo analysis for both AlphaFold2 and Swiss-Model with global scores of 0.55 ± 0.05 and 0.56 ± 0.05 , respectively (Fig EV2B and C) (Studer *et al*, 2020; Jumper *et al*, 2021). A direct comparison revealed an initial difference of 3.5 Å root-mean-square deviation (RMSD) in atomic positions between the structures. Closer inspection revealed several residues in the central pore that were hydrophobically buried in one model but exposed to the hydrophilic pore in the other (Fig EV2D). Therefore, we decided to test both models in this study.

Each of the apo models was individually embedded in a $86 \times 86 \text{ \AA}^2$ swatch of lipid bilayer using Charmm-GUI that recapitulated the composition of phospholipid components in mammalian inner mitochondrial membrane (POPC:POPE:CL = 2:3:2) (Comte *et al*, 1976; Jo *et al*, 2008; Wu *et al*, 2014; Mejia & Hatch, 2015; Lee *et al*, 2016). The system was hydrated and modeled with an ionic concentration of 150 mM KCl. Each model was analyzed in triplicate, and each replicate was $\sim 1 \mu\text{s}$ in duration (Table EV1). We observed that the mean RMSD over time among the replicates for both stabilized c-state models were 4.1 ± 0.3 and $2.9 \pm 0.2 \text{ \AA}$ for the Swiss-Model and AlphaFold2 models, respectively (Fig EV2E and F, Table EV1). In parallel, as a control for the approach, we generated a homology model for c-state human SLC25A4 (ANT1, ADP/ATP carrier) based on the solved bovine structure (PDB ID: 1OKC) (Pebay-Peyroula *et al*, 2003). The model for SLC25A4 (RMSD 2.8 Å) displayed a similar stability compared to the SLC25A51 c-state models over the course of the simulations (Fig EV2G). We further calculated root-mean-square fluctuation (RMSF) values for all c-state models, and as expected, observed less flexibility in transmembrane regions compared to loop regions (Fig EV2H–J). Together, the data indicated that the experimental model systems were stable.

Cardiolipin is required for SLC25A51 activity

With both the AlphaFold2 and Swiss-Model models, we observed spontaneous recruitment of cardiolipin molecules to three sites on SLC25A51 (Fig 1A, Movie EV1). Notably, all lipids were initially positioned at random and cardiolipin molecules were not docked to SLC25A51. We observed cardiolipin molecules arriving from different initial positions, displacing other types of phospholipids, and consistently interacting at the same three distinct sites on SLC25A51.

Cardiolipin binding was mediated by polar interactions between its phosphates and exterior-facing residues on the transporter at Binding Site 1 (T65, R66, R270, and G271), Binding Site 2 (N156,

T157, R82, and G83), and Binding Site 3 (S249, R174, G175) (Fig 1B). The observed sites correlated in position with cardiolipin binding motifs [F/Y/W] X G and [F/Y/W] [K/R] G identified from ADP/ATP transporter studies (Pebay-Peyroula *et al*, 2003; Nury *et al*, 2005; Ruprecht *et al*, 2014, 2019; Crichton *et al*, 2015; Duncan *et al*, 2018; Senoo *et al*, 2020; preprint: Senoo *et al*, 2023). All binding sites were on the exterior of the central pore facing the matrix leaflet and positioned at the junctions between the three repeated protein domains that comprised SLC25A51's pore (Fig 1A and B). Each cardiolipin molecule spanned an even-numbered helix from one domain and the matrix helix of the neighboring domain. At sites 1 and 3, cardiolipin bridged adjacent domains through extensive engagement of each of its phosphates (Fig 1B). At Site 2, a single phosphate of the cardiolipin molecule bridged the domains in 3 out of 4 replicates (Fig 1B). This suggested at least two binding modalities for cardiolipin and that cardiolipin may engage SLC25A51 asymmetrically. The dynamic and asymmetric recruitment of cardiolipin may be needed for matching the asymmetric shape of NAD^+ or to create flexibility in the pore SLC25A51; binding sites with distinct roles have been recently described in the ADP/ATP carrier (Mao *et al*, 2021; Yi *et al*, 2022; preprint: Senoo *et al*, 2023).

We introduced point mutations R82Q, R174Q, and R270Q at conserved residues to blunt the predicted electrostatic interactions at each binding site (Fig EV1B). These sites were exterior to the transporter's pore, distinct from the active site, and not obviously involved in interhelical interactions. Flag-SLC25A51 and Flag-SLC25A51^{R82Q-R174Q-R270Q} were detectable via Western blot and each co-localized with mitochondrial inner membrane protein Cox IV using immunofluorescence assays (Figs 1C and EV3A and B). We compared binding of immunoprecipitated Flag-SLC25A51 and Flag-SLC25A51^{R82Q-R174Q-R270Q} to cardiolipin-conjugated beads *in vitro* and found that the mutations diminished binding (Fig 1D).

To determine whether cardiolipin binding was required for SLC25A51 activity, we monitored SLC25A51-dependent uptake of $^{32}\text{P-NAD}^+$ (Eller *et al*, 2023) by adopting an assay previously used to characterize mitochondrial ADP/ATP transporter activity in bacterial cells (Haferkamp *et al*, 2002; Ravaut *et al*, 2012; Mifsud *et al*, 2013). The induced expression of SLC25A51 variants in *E. coli* cells resulted in their localization to the membrane fraction (Fig EV3C and D), reported to contain 5–10% cardiolipin (Dowhan, 1997). We observed a time-dependent internalization of $^{32}\text{P-NAD}^+$ upon induction of wildtype SLC25A51 (amino acids 29–297) but not with control cells expressing a predicted binding pocket mutant of SLC25A51 (Fig EV3E). Mutation of cardiolipin binding sites resulted in significantly less uptake compared to wildtype after 1 h (Fig 1E and F).

To determine whether cardiolipin binding impacted SLC25A51 activity in intact cells, we expressed a genetically encoded single fluorescent-protein ratiometric sensor for free NAD^+ in the mitochondria of HeLa cells (Cambronne *et al*, 2016; Eller *et al*, 2019; Luongo *et al*, 2020). Figure 1G depicts the inverted fluorescence intensity of the sensor that is a readout of relative NAD^+ concentrations. Acute ectopic expression of Flag-SLC25A51 resulted in increased steady-state levels of free mitochondrial NAD^+ compared to empty vector, demonstrating that this assay could measure the activity of SLC25A51 of importing NAD^+ in intact and respiring cells (Fig 1G). Flag-SLC25A51^{R82Q-R174Q-R270Q} was unable to efficiently increase mitochondrial NAD^+ concentrations indicating that cardiolipin binding was

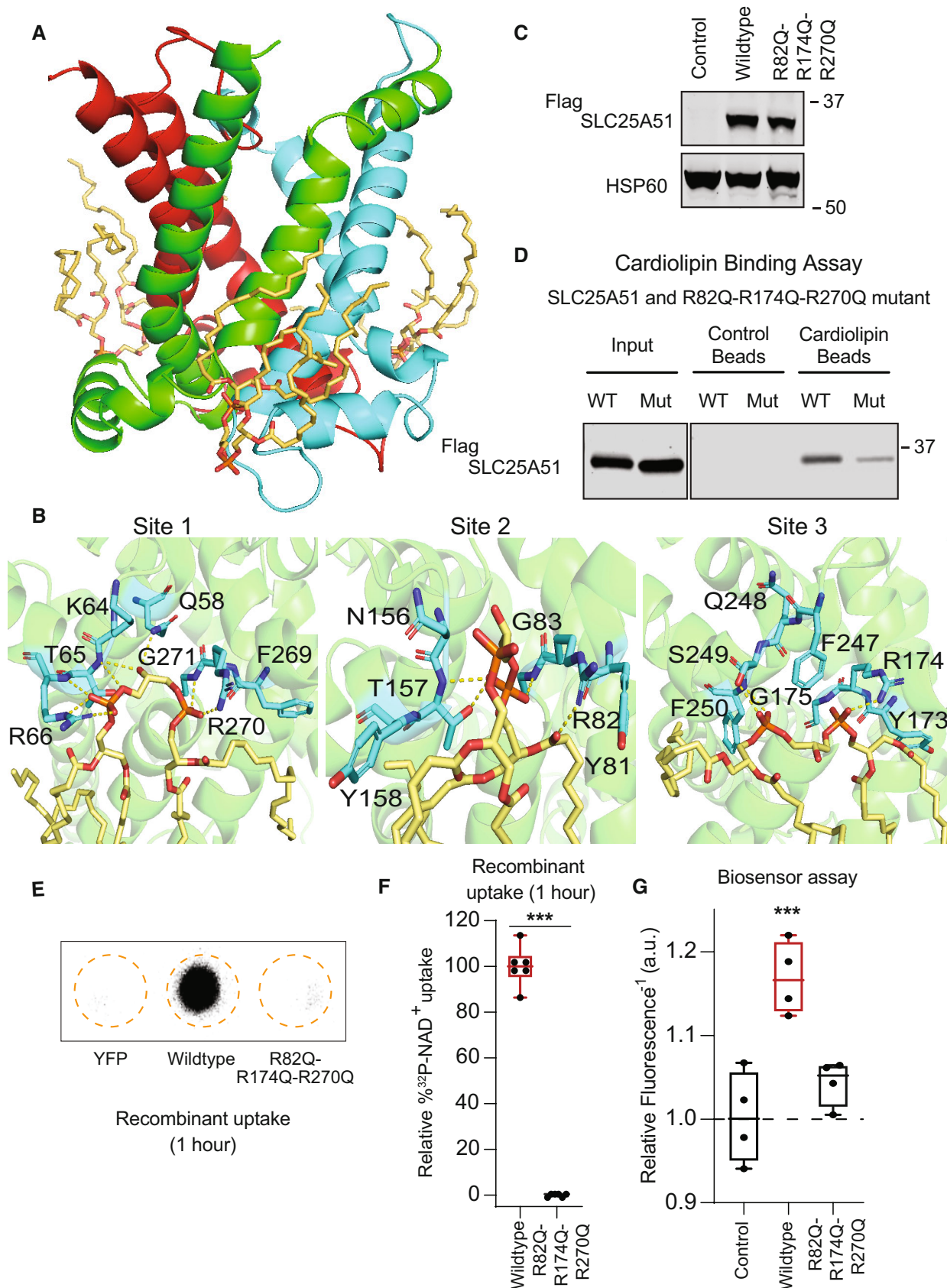


Figure 1.

Figure 1. Cardiolipin binding impacts SLC25A51 function.

- A Cardiolipin (wheat) bound to SLC25A51 at the junctions of its repeated domains, highlighted in red, green, and blue.
- B Representative poses depicting identified interactions at sites 1–3. Yellow dashes indicate interactions $< 3.5 \text{ \AA}$. At site 2, the binding of a single cardiolipin phosphate was observed.
- C Anti-Flag Western blot for transiently transfected ^{Flag}SLC25A51 variants and empty vector control in HeLa cells; HSP60, loading control.
- D *In vitro* pull down of ^{Flag}SLC25A51 variants using cardiolipin-bound or control beads and detected with anti-Flag Western blots.
- E Representative phosphorimage of ³²P-NAD⁺ taken up after 1 h in recombinant *E. coli* cells expressing indicated SLC25A51 variants (amino acids 29–297) or negative control protein YFP.
- F Quantitation of ³²P-NAD⁺ uptake after 1 h in *E. coli* cells expressing wildtype SLC25A51 (amino acids 29–297, red) and the indicated mutant. Data are shown in box and whisker format, with hinges at 25th and 75th percentiles, whiskers represent min and max and the line is the median, $n = 6$ biological replicates, unpaired two-sided t -test $***P < 0.001$.
- G Free mitochondrial NAD⁺ levels measured using a ratiometric biosensor in HeLa cells co-expressing empty vector control or ^{Flag}SLC25A51 variants. Measurements were taken at 24 h post-transfection; the dashed line indicates the baseline defined by the empty vector control, and red denotes data equivalent to wildtype. Data are shown in box and whisker format, with hinges at 25th and 75th percentiles, whiskers represent min and max and the line is the median, $n = 4$ biological replicates, ANOVA < 0.01 with post-hoc Dunnett's Test compared to empty vector control, $***P < 0.001$.

Source data are available online for this figure.

required for SLC25A51 function (Fig 1G). We observed a similar loss of activity compared to wildtype when Flag-SLC25A51^{R82Q-R174Q-R270Q} was expressed in HEK293 SLC25A51 Knockout (KO) line (Fig EV3F and G).

The matrix gate is comprised of a single salt bridge interaction

To study the control of SLC25A51 opening to the matrix, we examined all possible inter-helical interactions at the position where gated salt-bridge networks have been identified in the related MCF carriers (Nelson *et al*, 1998; Ruprecht & Kunji, 2021; Ziegler *et al*, 2021). In SLC25A51, there were only two potential interhelical interactions: a putative hydrogen bond between Q52 and Q142, and a putative ionic salt-bridge between E139 and K236 (Fig 2A). Time evolution of each interaction over 1,000 ns in both AlphaFold2 and Swiss-Model models indicated that the hydrogen bond (Q52-Q142) was not formed (combined mean percent occupancy, m.p.o. $2\% \pm 0.7\%$) while the salt bridge interaction (E139-K236) was stable (combined m.p.o., $93\% \pm 3\%$) (Fig 2B and C).

We used the mitochondrial NAD⁺ sensor assay and an *E. coli* uptake assay to test whether these interactions were required for SLC25A51 activity. Loss of the gate is predicted to favor the inward-facing, matrix (m-state) conformation, which would not be amenable to NAD⁺ import. Expression of SLC25A51 variants in HeLa cells with an ablated salt bridge (K236Q, K236A, E139Q, or E139A point mutations) were not able to increase steady-state levels of free mitochondrial NAD⁺ levels compared to empty vector control (Fig 2D). We also tested the K236Q mutation in HEK293 SLC25A51 KO cells and observed no significant mitochondrial NAD⁺ increase (Fig EV3H). This indicated that formation of the E139-K236 salt bridge was required for SLC25A51 activity. In line with the simulation results, disruption of the putative hydrogen bond with Q52A or Q142A did not have any major impact on SLC25A51 activity (Fig 2D). Furthermore, conserved residues in the consensus matrix gate motif (PX[D/E]XX[K/R]XXQ)—including L55 and N233 whose counterparts were identified as critical in the yeast and plant mitochondrial carriers (Miniero *et al*, 2022)—were not required for SLC25A51 activity in cells (Fig 2D). We further confirmed the necessity of the salt bridge using uptake assays and found that introduction of either E139Q-K236Q or K236Q mutations resulted in loss of activity (Figs 2E and F, and EV3I). Together, the modeling and

the biochemical assays indicated that a single interhelical salt-bridge between E139 and K236 formed the matrix gate.

Glutamine braces are not required for SLC25A51 activity

In many MCF carriers, glutamine braces play important roles in regulating the matrix gate (Ruprecht & Kunji, 2021). We observed an analogously positioned glutamine residue Q240 in SLC25A51 to putatively brace the identified E139-K236 salt-bridge (Fig 2A and B). Modeling analyses were used to test the stability of either a Q240-E139 or Q240-K236 interaction. We did not observe consistent interactions in either model (Q240-E139 combined m.p.o. of $5\% \pm 3\%$; Q240-K236 combined m.p.o. of $45\% \pm 16\%$) (Fig 2G). In agreement, mutation of Q240, or analogous glutamine residues Q59 and Q146 in adjacent domains, minimally impaired SLC25A51 activity (Figs 2D–F and EV3I). Together, our data demonstrated that the identified salt-bridge gate in SLC25A51 can function without stabilization from glutamine braces, distinctly unique from many other MCF carriers (Ruprecht & Kunji, 2021).

Arginine cap residues contribute to regulating SLC25A51 activity

Cap residues at the matrix opening of the transporter have been proposed to help stabilize the c-state of MCF carriers by neutralizing c-terminal negative dipoles of converging odd-numbered helices or by forming stabilizing ionic interactions with matrix helices (Pierri *et al*, 2014; Yi *et al*, 2019). While modeling SLC25A51, we observed three arginine residues, R57, R238, and R140, positioned to putatively serve as cap residues (Fig EV4A). Mutation of each of the three cap residues (R57L, R140L and R238L) partially impaired SLC25A51 activity (Fig EV4B). In agreement, we observed stable interactions over time between R140 and the backbone of residue Q240 (m.p.o. $95\% \pm 3\%$ AlphaFold2 model, m.p.o. $80\% \pm 16\%$ Swiss-Model), as well as between R238 and the backbone of residue Q59 (m.p.o. $70\% \pm 10\%$, Swiss-Model).

NAD⁺ import can occur independently of a stable cytoplasmic gate

SLC25A51 is predicted to function via an alternating-access mechanism similarly to other MCF family members (Robinson *et al*, 2008;

Ziegler et al, 2021; Cimadamore-Werthein et al, 2023). We thus generated an m-state model (MolProbity 94th percentile)—using Swiss-Homology Modeling and the solved structure of *T. thermophila* ADP/ATP carrier (PDB ID: 6GCI) (Ruprecht et al, 2019)—to help identify the cytoplasmic gate. Performed in

triplicate (~ 1 μs/replicate, Table EV1), we observed consistent and stable formation of a putative ionic gate between K198 and E291 (m.p.o. 95% ± 5%) in an analogous plane to the identified cytoplasmic gate in the ADP/ATP carrier (Fig EV4C and D). This suggested that SLC25A51 has single salt bridge gates on each side of

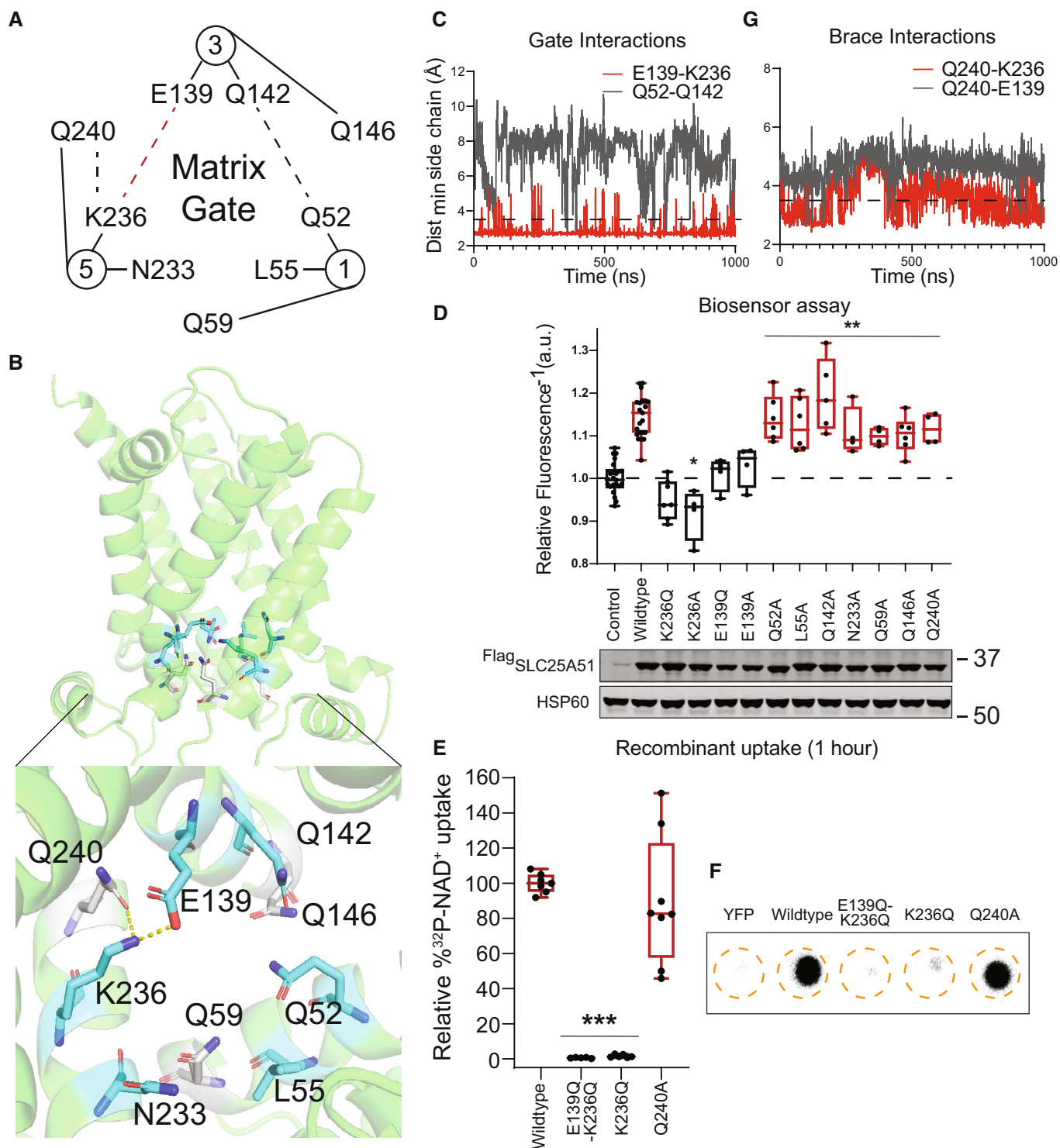


Figure 2.

Figure 2. A single salt bridge stabilizes the NAD⁺-accessible, outward facing conformation.

- A Graphical representation of the matrix gate with dash lines indicating possible polar non-covalent interactions. Interactions were either indicated (red) or unsupported (gray) by data.
- B Relative position of the matrix gate in a cartoon representation of SLC25A51; tested glutamine brace residues (white) and interactions (dashed lines).
- C Time evolution of distance between indicated side chains for putative gate interactions. Interaction cutoff of 3.5 Å is shown as a dashed line.
- D Free mitochondrial NAD⁺ levels measured using a ratiometric biosensor in HeLa cells expressing empty vector control ($n = 25$ biological replicates), wildtype ^{Flag}SLC25A51 ($n = 25$ biological replicates), and indicated mutants ($n = 4–6$ biological replicates). Measurements were taken at 24 h post-transfection; the dashed line indicates the baseline defined by the empty vector control, and red denotes data equivalent to wildtype. Data are shown in box and whisker format, with hinges at 25th and 75th percentiles, whiskers represent min and max and the line is the median, ANOVA $P < 0.0001$ with post-hoc Dunnett's test compared to empty vector control, * $P < 0.05$, ** $P < 0.01$. (bottom) Protein expression from HeLa cells transiently transfected with empty vector control, wildtype ^{Flag}SLC25A51 and the indicated variants using anti-Flag Western blot; HSP60, loading control.
- E Quantitation of uptake of ³²P-NAD⁺ after 1 h by *E. coli* cells expressing wildtype SLC25A51 (amino acids 29–297) and the indicated mutants; wildtype activity and equivalent, red. Data are shown in box and whisker format, with hinges at 25th and 75th percentiles, whiskers represent min and max and the line is the median, $n = 5–8$ biological replicates, ANOVA $P < 0.0001$ with post-hoc Dunnett's test compared to wildtype, *** $P < 0.001$.
- F Representative phosphorimage of ³²P-NAD⁺ taken up after 1 h in recombinant *E. coli* cells expressing indicated SLC25A51 variants (amino acids 29–297) or negative control protein YFP.
- G Time evolution of distance between indicated side chains of putative brace interactions. Interaction cutoff at 3.5 Å is shown as a dashed line.
- Source data are available online for this figure.

its pore. Mutation of the cytoplasmic gate is expected to favor the c-state conformation. Interestingly, introduction of double mutations K198Q-E291Q or K198A-E291A did not impair SLC25A51 activity (Fig EV4E–H) unlike previously observed for ADP/ATP carrier (King *et al.*, 2016; Ruprecht *et al.*, 2019). This indicated that a c-state conformation was sufficient for importing NAD⁺ and that a stable m-state was not required for continuous uptake of NAD⁺. This capacity for uniport was previously predicted based on relative strengths of the gates (Robinson *et al.*, 2008).

Putative tyrosine brace interactions were also observed but with lowered percent occupancy (E103-Y290 m.p.o. 68% ± 24%; R194-E291 m.p.o. 63% ± 8.5%) (Fig EV4C and D). In agreement with the idea that a stable m-state was not essential, many of the disruptive mutations had minimal effect on SLC25A51 activity (Fig EV4E). The exception was that R194A and R194Y blocked SLC25A51 activity; however, mutation of its binding partner E291 did not result in any impairment, so any contribution from R194 was likely independent of its brace function. Together, the data indicated that cytoplasmic gate and brace features were not critical to SLC25A51's import function.

NAD⁺ is orientated by charge to bind at three conserved contact points

To study how SLC25A51 engages its ligand, we unbiasedly modeled the binding of NAD⁺ onto both c-state models. We used the AutoDock 4.2 algorithm (Morris *et al.*, 2009; Forli *et al.*, 2016) to generate a series of poses ordered by calculated binding energy scores. We chose the poses with the lowest binding energy scores from each model to continue with analyses using MD simulations.

With both models (Table EV1 Simulations 10–18), we observed a prompt (within 100 ns) and consistent positioning of the nicotinamide ring (Fig 3A and B, Movies EV2 and EV3). The central ligand-binding pore of SLC25A51 is characterized by positive charges arising from inward facing residues K91, R182, and R278 on the even-numbered helices, and a distinct negatively charged region from acidic residue E132 on helix 3 (Fig 3A). We observed in both models that the positively-charged nicotinamide ring of oxidized NAD⁺ consistently oriented away from the basic residues in the binding site

and toward E132 (Fig 3A and B, Movies EV2 and EV3). Ablation of E132's charge impaired SLC25A51 activity, but a E132D variant retained function (Figs 3C and F, and EV3I and J). E132 is conserved across SLC25A51 orthologs (Fig EV1B).

We had previously determined that the presence of an equal concentration of NADH (100 μM) did not significantly interfere with SLC25A51 uptake activity of NAD⁺ (Fig 3D) (Luongo *et al.*, 2020). A positive charge in the nicotinamide ring structure is a feature that distinguishes the oxidized form of NAD⁺ from reduced NADH. We hypothesized that electrostatic charges may facilitate an interaction between NAD⁺ and E132 in the pore of SLC25A51. To test this, we compared the ability for either unlabeled NAD⁺ or NADH to compete for SLC25A51-dependent uptake of ³²P-NAD⁺ either at equivalent (100 μM) or 2.5-fold higher concentrations (250 μM). With both concentrations, oxidized NAD⁺ successfully competed and impeded ³²P-NAD⁺ uptake (Fig 3D). With wildtype SLC25A51, oxidized NAD⁺ was a significantly better competitor compared to NADH. However, loss of E132 resulted in a loss of discrimination for SLC25A51 between NAD⁺ and NADH when ligands were present at equal concentrations (Fig 3D). This suggests that E132 contributes to ligand selectivity. The relatively subtle E132 may be enough to create a molecular discrimination based on electrostatic charge, given the much higher concentrations of NAD⁺ compared to NADH available for import in mitochondria. Free cytosolic NAD⁺ is approximately 100 to 1,000-fold more abundant than free NADH (Williamson *et al.*, 1967; Zhang *et al.*, 2002; Hung *et al.*, 2011; Zhao *et al.*, 2011). Cytosolic ratios—which due to non-discriminating porin channels in the outer membrane—likely represent what is experienced by intracellular SLC25A51.

We observed the nicotinamide ribose (NR) moiety formed consistent contacts (in 8 out of 9 simulations with both Swiss-Model and AlphaFold2 models) (Table EV1). Borrowing the terminology used in the ADP/ATP binding pocket (Kunji & Robinson, 2006; Robinson & Kunji, 2006; Robinson *et al.*, 2008), we observed that SLC25A51 used residue T94 in contact site 1 and N183 in contact site 2 to stabilize the NR moiety through specific hydrogen bonds with its carboxamide group and ribose (2' and 3' OH), respectively (Fig 3E). R278 in contact site 3, R182, and K91 engaged the negative charges from the phosphates of NAD⁺ (Fig 3E, Movies EV2 and EV3).

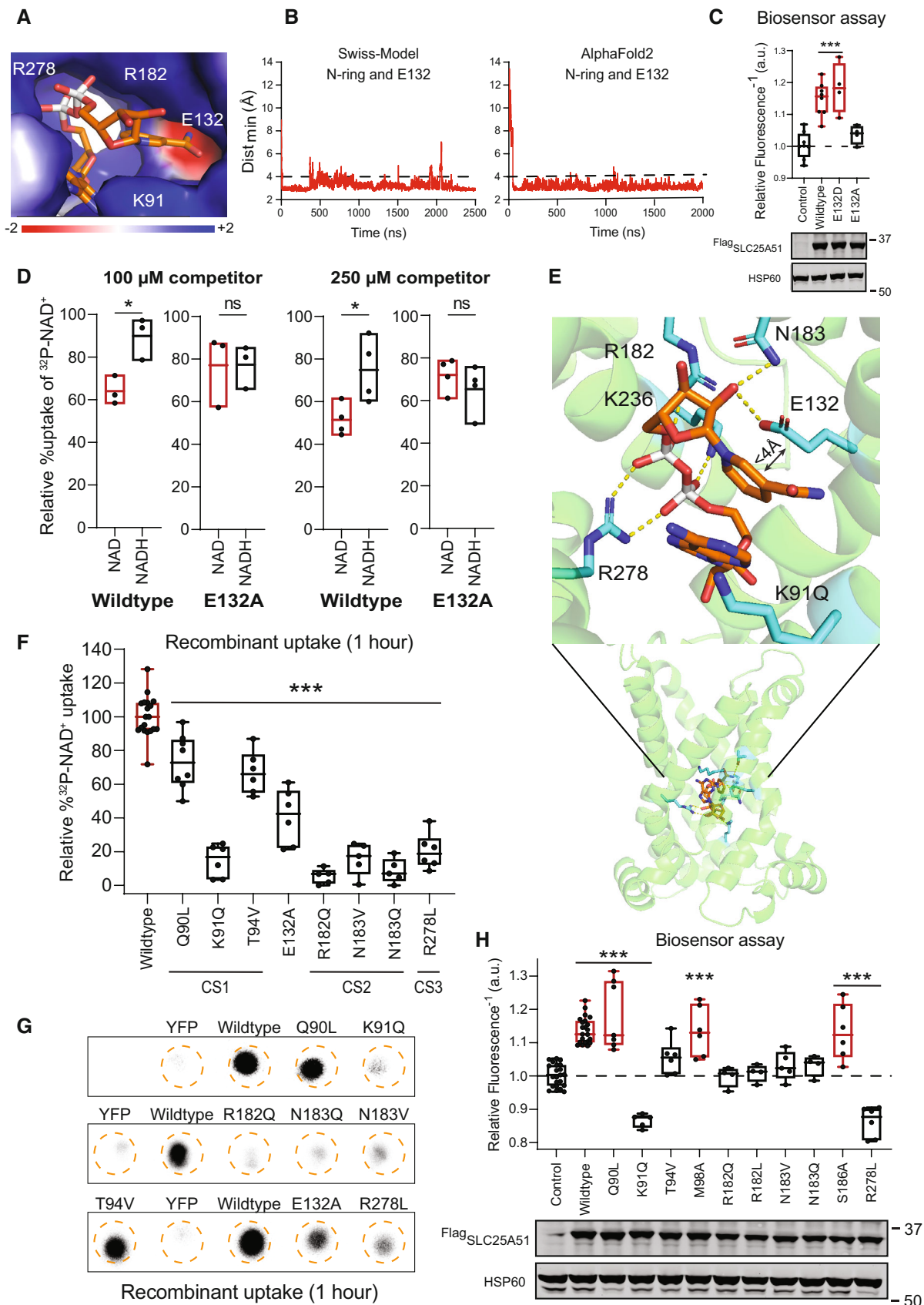


Figure 3.

Figure 3. E132 and conserved contact sites comprise a selective NAD⁺ binding site.

- A Electrostatic environment of the substrate binding site (APBS as Pymol plugin). Representative positioning of NAD⁺ from simulation 17 at 1,230 ns (Table EV1).
- B Minimal distance over time between the nicotinamide ring and E132 in simulations 17 (Swiss-Model) and 12 (AlphaFold2) (Table EV1). Interaction cutoff at 4 Å shown as a dashed line.
- C Free mitochondrial NAD⁺ levels measured using a ratiometric biosensor in HeLa cells co-expressing empty vector control ($n = 8$ biological replicates), wildtype ^{Flag}SLC25A51 ($n = 8$ biological replicates), and indicated mutants ($n = 4$ biological replicates). Measurements were taken at 24 h post-transfection; the dashed line indicates the baseline defined by the empty vector control, and red denotes data equivalent to wildtype. Data are shown in box and whisker format, with hinges at 25th and 75th percentiles, whiskers represent min and max and the line is the median, ANOVA $P < 0.0001$ with post-hoc Dunnett's test compared to empty vector control *** $P < 0.001$. (bottom) Protein expression from HeLa cells transiently transfected with empty vector control, wildtype ^{Flag}SLC25A51 and the indicated variants using anti-Flag Western blot; HSP60, loading control.
- D Relative uptake of ³²P-NAD⁺ after 1 h by *E. coli* cells expressing wildtype SLC25A51 (amino acids 29–297) or the E132A mutant when competed by 100 μM ($n = 3$ biological replicates) and 250 μM ($n = 4$ biological replicates) unlabeled NAD⁺ (red) or NADH (black). Data is shown as floating bars with central line at mean and the box represents the min and max value, unpaired two-sided t -test * $P < 0.05$.
- E Bound NAD⁺ (orange) in the ligand binding pocket (cyan) is shown in both side and enlarged views. Non-covalent interactions < 3.5 Å, dashed yellow lines.
- F Quantitation of ³²P-NAD⁺ uptake after 1 h in *E. coli* cells expressing wildtype SLC25A51 (amino acids 29–297) and indicated mutants; wildtype activity ($n = 19$ biological replicates) and equivalent, red. Data are shown in box and whisker format, with hinges at 25th and 75th percentiles, whiskers represent min and max and the line is the median, $n = 5$ –8 biological replicates, ANOVA $P < 0.0001$ with post-hoc Dunnett's test compared to wildtype *** $P < 0.001$.
- G Representative phosphorimage of retained ³²P-NAD⁺ after 1 h by *E. coli* cells expressing wildtype SLC25A51 (amino acids 29–297), indicated variants, or YFP control.
- H Free mitochondrial NAD⁺ levels measured using a ratiometric biosensor in HeLa cells expressing empty vector control ($n = 27$ biological replicates), wildtype ^{Flag}SLC25A51 ($n = 27$ biological replicates), and indicated mutants ($n = 4$ –7 biological replicates). Measurements were taken at 24 h post-transfection; the dashed line indicates the baseline defined by the empty vector control, and red denotes data equivalent to wildtype. Data are shown in box and whisker format, with hinges at 25th and 75th percentiles, whiskers represent min and max and the line is the median, ANOVA $P < 0.0001$, post-hoc Dunnett's test compared to empty vector control *** $P < 0.001$. (bottom) Protein expression from HeLa cells transiently transfected with empty vector control, wildtype ^{Flag}SLC25A51 and the indicated variants detected by anti-Flag Western blot; HSP60, loading control.

Source data are available online for this figure.

We mutated and tested the requirement of conserved residues in the three contact sites using the sensor and uptake assays (Figs 3F–H, EV1B and EV3I and J) (Ruprecht & Kunji, 2021; Ziegler et al, 2021). For contact site 1, we found that SLC25A51 variants with a K91Q mutation—and to a lesser extent T94V—impaired SLC25A51 import with minimal effects on protein stability. Mutating adjacent contact site residues (Q90 and M98) that were not observed to participate in binding of the NR moiety minimally impaired SLC25A51 despite being conserved residues (Figs 3F–H, EV1B and EV3I and J). Similarly, we confirmed that R182 and N183 were required for site 2 but not neighboring residue S186, and R278 was required for site 3 (Figs 3F–H and EV3I and J). The results were consistent with previous docking and mutational analyses (Kory et al, 2020; Ziegler et al, 2021). We observed that all three contact sites in SLC25A51's pore must be engaged to orient the ligand such that it can travel deeper into the pore. This may explain why nicotinamide, or its mononucleotide were unable to efficiently compete with NAD⁺ for transport (Kory et al, 2020; Luongo et al, 2020).

NAD⁺ directly engaged with the gate in SLC25A51

While modeling the binding of NAD⁺, we unexpectedly observed two simulations wherein the ligand traversed deeper into the pore (Movie EV4 and Table EV1 simulations 16 and 17). To determine whether an extended simulation could provide additional insights, we continued with a pose that originated from the unbiased docking with the Swiss-Homology model but had scored among lowest binding energy scores (Table EV1 simulations 19–22). This pose positioned the nicotinamide ring deeper in the pocket.

In all four replicate simulations 19–22, we observed channeling of the nicotinamide ring from E132 to E139 (Fig 4A and B, Movie EV4). This was reminiscent of the electrostatic funneling observed with ADP/ATP carriers (Heidkämper et al, 1996; Dehez et al, 2008; Wang & Tajkhorshid, 2008; Krammer et al, 2009; Monné et al, 2013;

Mavridou et al, 2022). In both model structures, residue E139 of the salt-bridge gate was positioned below E132 on the same helix 3. We also observed that as the nicotinamide ring interacted with E139 (85, 48, 69 and 93% occupancy), the phosphates on NAD⁺ could interact with K236, the other half of the salt bridge. Resultingly, formation of the E139-K236 salt bridge was negatively correlated with the NAD⁺ phosphate-K236 interaction ($R = -0.192, -0.045, -0.681$ and -0.336 per replicate, $P < 0.001$), as well as with the nicotinamide ring-E139 interaction ($R = -0.298, -0.053, -0.091$ and -0.342 calculated per replicate, $P < 0.001$) (Fig 4C and D, Movie EV5). Together this disrupted an otherwise stable gate interaction (Fig 4, Movie EV5). An analogous ligand-initiated mechanism has been proposed for the ADP/ATP carrier involving interference of the gate via the N6 atom of the adenine moiety on the nucleotide or the guanidino NH1 or NH2 of a conserved binding site arginine residue (Kunji & Robinson, 2006).

Previously, studies showed that AMP, dUTP, NADH, GDP and GTP can bind the ADP/ATP carrier, suggesting that the dynamics of transport in cells involves an additional differentiation step to discriminate between bound molecules (Mifsud et al, 2013; Majd et al, 2018). To determine the requirement of the alignment between E132 and E139 for activity we reversed the positioning of E139 with its salt bridge (E139K-K236E) and tested SLC25A51 activity using sensor assays. We also shifted the position of the entire salt bridge so that it was misaligned (E139Q-K236Q-Q52E-Q142K). Activity was lost in the cases where the position of E139 was reversed or shifted, indicating that the alignment of this residue was critical (Fig 4E). We also introduced an additional salt bridge (Q52E-Q142K), while maintaining the original salt bridge. The presence of an extra constitutive salt-bridge that did not have an established regulatory mechanism resulted in significant loss of SLC25A51 activity (Fig 4E). Nevertheless, SLC25A51 activity was not fully diminished. The residual activity indicated that the preserved E132/E139 alignment was functional but that its role was partially hampered by the extra

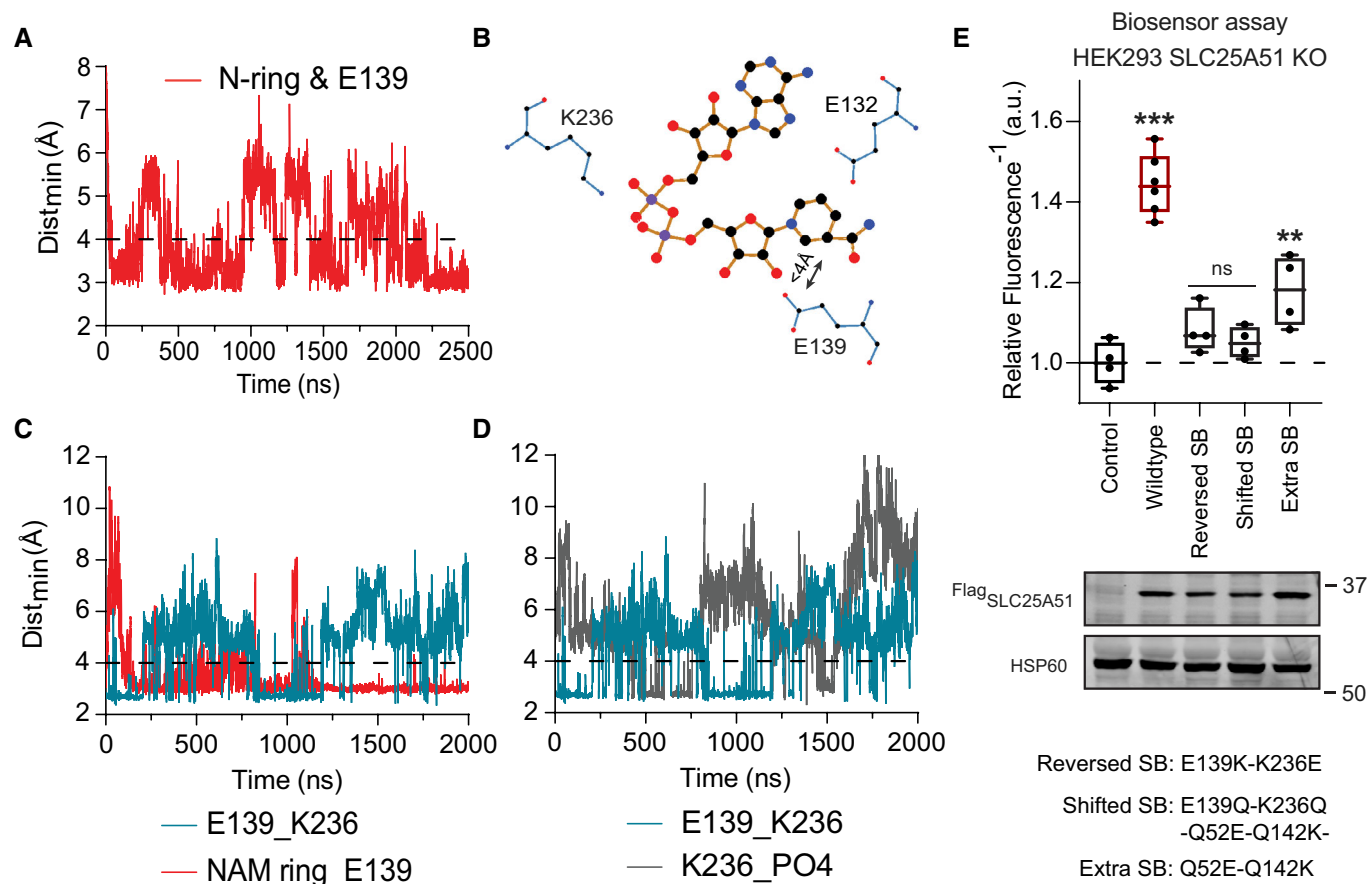


Figure 4. Substrate induced disruption of the matrix gate.

- A Minimum distance between the nicotinamide ring and E139 over time, simulation 17 (Table EV1). Interaction cutoff at 4 Å is shown as a dashed line.
- B Two-dimensional projection (Ligplot+) of NAD⁺ and its interaction with E132 and the E139-K236 salt bridge.
- C Time evolutions of the E139-K236 salt bridge (teal) compared to the nicotinamide ring and E139 interaction (red); simulation 19 (Table EV1). Interaction cutoff at 4 Å is shown as a dashed line.
- D Time evolutions of the E139-K236 salt bridge (teal) compared to the phosphates in NAD⁺ and K236 (gray); simulation 19 (Table EV1). Interaction cutoff at 4 Å is shown as a dashed line.
- E Free mitochondrial NAD⁺ levels measured using a ratiometric biosensor in HEK293 SLC25A51 KO cells expressing empty vector control, wildtype Fl^{ag}SLC25A51, and indicated mutants. Measurements were taken at 48 h post-transfection; the dashed line indicates the baseline defined by the empty vector control, and red denotes data equivalent to wildtype. Data are shown in box and whisker format, with hinges at 25th and 75th percentiles, whiskers represent min and max and the line is the median, $n = 4-6$ biological replicates, ANOVA $P < 0.0001$, post-hoc Dunnett's test compared to empty vector control $**P < 0.01$, $***P < 0.001$. (bottom) Protein expression from HEK293 SLC25A51 KO cells transiently transfected with empty vector control, wildtype Fl^{ag}SLC25A51 and the indicated variants detected with anti-Flag Western blot; HSP60, loading control.

Source data are available online for this figure.

salt bridge (Fig 4E). Together, the data suggest that alignment of E132/E139 functions to facilitate gate opening.

With this study, we have gained insight into how the binding pocket of SLC25A51 aids the selective transport of oxidized NAD⁺, as well as evidence for ligand-induced gate opening. The preference for NAD⁺ implies SLC25A51 can alter flux through the tricarboxylic acid cycle by controlling the local NAD⁺/NADH ratio and oxidoreductive reactions. As specific point mutations can partially destabilize SLC25A51, we have sought corroborating data from multiple independent assays. A limitation is that a fully *in vitro* reconstitution of SLC25A51 activity has yet to be achieved. Future elucidation of the full dynamics of SLC25A51 will accelerate the development of SLC25A51 modulators for targeting disease (Fig EV5).

Materials and Methods

Multiple sequence alignment

Multiple Sequence Alignment was performed using Cobalt sequence alignment tool (Papadopoulos & Agarwala, 2007) and was viewed and analyzed using Unipro UGENE (Okonechnikov *et al*, 2012). Figure EV1A depicts the alignment of representative nucleotide carriers HsSLC25A51 (UniProt: Q9H1U9), BtSLC25A4 (UniProt: P02722, PDB ID: 1OKC), TtADT (UniProt: G2QNH0, PDB ID: 6GCI), ScNdt1 (UniProt: P40556) and AtNdt1 (UniProt: O22261). Figure EV1B shows the alignment for the following SLC25A51 homologs and paralogue: human SLC25A51 (UniProt: Q9H1U9), human SLC25A52

(UniProt: Q3SY17), mouse SLC25A51 (UniProt: Q5HZI9), drosophila SLC25A51 (UniProt: Q7K483), zebrafish SLC25A51 (UniProt: Q6PBV5), xenopus SLC25A51 (UniProt: A9UMI0) and snake SLC25A51 (UniProt: A0A6P9B6W2).

SLC25A51 models

The homology models of cytoplasmic open state of apo-SLC25A51 (amino acids 27–297) and apo-SLC25A4 were generated using the Swiss-Model server with bovine SLC25A4 crystal structure as the template (PDB ID: 1OKC) (Pebay-Peyroula *et al.*, 2003; Waterhouse *et al.*, 2018). Bovine SLC25A4 was chosen as it has a high-resolution crystal structure available (2.2 Å) and its GMQE score of 0.55 was the highest for SLC25A51 among all the c-state MCF carrier structures available. The homology model of mitochondrial matrix open state of apo-SLC25A51 (amino acids 26–297) was generated using the Swiss-Model server with a thermophilic fungal ADP/ATP Carrier crystal structure as the template (PDB ID: 6GCI) (Ruprecht *et al.*, 2019). We also used AlphaFold2 generated cytoplasmic open state model for our study (Jumper *et al.*, 2021). The SLC25A51 models quality estimation was performed using MolProbity, pLDDT scores and QMEANDisCo analysis (Williams *et al.*, 2018; Studer *et al.*, 2020; Jumper *et al.*, 2021).

Setup used in molecular dynamics simulations

CharmmGUI webserver was used to build the starting coordinates of our system for MD simulations with a total dimension of 85 Å × 85 Å × 100 Å (Jo *et al.*, 2007; Wu *et al.*, 2014). The c-state Swiss-Model (apo-state or NAD⁺ docked), m-state Swiss-Model and apo-c-state AlphaFold2 SLC25A51 were embedded in lipid bilayer systems with phosphatidylcholine (POPC), phosphatidylethanolamine (POPE) and cardiolipin (TLCL2) in a ratio 2:3:2 as experimentally determined previously (Comte *et al.*, 1976). We chose TLCL2 cardiolipin with a negative 2 charge that agrees with the recent studies on ionization properties of the cardiolipin molecules (Olofsson & Sparr, 2013; Sathappa & Alder, 2016). The protein and the lipid bilayer were solvated with TIP3P water molecules extending up to 22.5 Å on both sides of the membrane. The system also contains neutralizing K⁺ and Cl⁻ ions to make the final salt concentration 150 mM. The NAD⁺ was docked on the final coordinate of SLC25A51 after 1 μs simulation of AlphaFold2 SLC25A51 model which was embedded in a lipid bilayer membrane of POPC lipids with all the other parameters same as the other models described above.

Molecular dynamics simulation

The simulations were performed with Gromacs (version 2022.1) using an all atom Charmm36m force field for protein, lipids, ions and ligands with periodic boundary conditions (Bekker *et al.*, 1993; Abraham *et al.*, 2015). We performed energy minimization of the system in 5,000 steps of steepest descent with position restraints on protein and NAD⁺ while lipids, water and ions were free to equilibrate. The system was equilibrated in a multi-step procedure with decreasing positional and dihedral constraints with each step with following parameters: Two steps of 0.125 ns NVT simulation at 310.15 K, one step of 0.125 ns NPT simulation at 310.15 K and 1 bar, and three steps of 0.5 ns NPT simulation at 310.15 K and 1 bar. MD

simulations were run for different lengths of time using leap-frog algorithm as an integrator with 2 fs time step. Particle Mesh Ewald was used for non-bonded long-range interactions with a 12 Å cutoff and Leonard-Jones potential cutoff was 12 Å. Temperature was maintained at 310.15 K using Nose-Hoover thermostat with a 1 ps coupling parameters and pressure at 1 bar using Parrinello-Rahman barostat with 5 ps coupling and 4.5×10^{-5} bar⁻¹ compressibility.

Trajectory analysis

The analysis was done using in-built tools available in the gromacs package. The coordinates were viewed, and structural graphics and videos were prepared using Pymol. The cutoff distance was 3.5 Å for hydrogen bonds and for salt bridges while 4 Å for distance between any atom of Nicotinamide ring of NAD⁺ and side chain of amino acid. The mean percentage occupancy (mpo) represents the percentage of simulation time where the distance between the atoms was under the cut-off distance. Time evolution of distances and RMSD is shown as moving averages of 5 values on each side. The videos are made with every 10th ns frame of the trajectories.

APBS electrostatics

APBS electrostatics was performed using Pymol plugin. The molecule was prepared using pdb2pqr method with 0.5 grid spacing and the electrostatic potential was projected to Connolly Surface in the -2 to +2 range.

Cell culture

HeLa (ATCC: CCL-2) and HEK293 (ATCC: CRL-1573) cells were cultured in Dulbecco's modified Eagle's medium (DMEM) containing 4.5 g/L glucose, 1 mM sodium pyruvate and 4 mM L-glutamine supplemented with 10% fetal bovine serum, 1× penicillin–streptomycin and 12.5 mM HEPES buffer (pH 7.4). Cell lines are tested monthly for mycoplasma contamination.

Cloning

SLC25A51 (amino acids 29–297) and YFP were cloned in pMW7 bacterial expression vector using NEBuilder[®] HiFi DNA Assembly Master Mix. Q5 site-directed mutagenesis kit from NEB was used to make mutations in pMW7-SLC25A51 (amino acids 29–297) plasmid and the pCMV-Flag-HA-SLC25A51 (amino acids 1–297)-IRES-puro plasmid (Luongo *et al.*, 2020).

Generation of HEK293 SLC25A51 knockout lines

CRISPR-Cas9-engineered HEK293 cells lacking a functional gene for SLC25A51 were generated as described before (Ran *et al.*, 2013). Briefly, hybridized oligonucleotides 5'- CACCGTAGTTGTCTTCTG CATCAA and 5'- AAAGTTGATGCAGAAGACAACACTAC were inserted into high-fidelity BbsI-digested plasmid pSpCas9(BB)-2A-Puro (PX459) V2.0 (Addgene #62988). A total of 800,000 HEK293 cells were seeded in a 6-well plate and after 24 h were transfected using X-tremeGENE 9. Twenty-four hours post transfection, about 5% each of the transfected cells were distributed onto 10 cm dishes and incubated with puromycin (2 μg/ml) for 48 h. Five to seven days

after puromycin withdrawal, cell clones were picked and expanded. Genome editing within the targeted genomic DNA sequence was confirmed after PCR amplification from isolated genomic DNA using primers 5'- TTGTGTGGCTGCTGTGCAGC and 5'- GAGCACTGTGAG TCGTTGCG followed by Sanger sequencing using the primer 5'- CTTTCGACAACAGCTGTATGG. We confirmed that the CRISPR-plasmid did not integrate itself by immunoblot analyses to monitor Flag-Cas9 expression and retention of puromycin sensitivity. The knockout of SLC25A51 was validated at protein level using Western blotting and at the genomic level by sequencing.

Generation of HEK293 SLC25A51 Knockout lines stably expressing NAD⁺ biosensor.

The lines were generated following a similar protocol used for HeLa sensor lines described previously (Luongo *et al*, 2020). We transduced HEK293 SLC25A51 knockout cell line with lenti virus encoding ^{Mito}cpVenus or ^{Mito}Sensor. Stable integration was selected with 10 µg/ml Blasticidin for 1 week. Cells were sorted for fluorescence and validated using sensor response to ^{Flag}SLC25A51 and ^{Flag}Ndt1 overexpression.

Mitochondrial steady state NAD⁺ measurements

The pCMV-Flag-HA-SLC25A51 (amino acids 1–297)-IRES-puro plasmids were transiently transfected:

- (i) HeLa ^{Mito}cpVenus and HeLa ^{Mito}Sensor cells using polyethylenimine (PEI, 1 mg/ml) with a PEI:DNA ratio of 5:1 and relative NAD⁺ steady state measurements were taken 24 h post-transfection using flow cytometry.
- (ii) HEK293 SLC25A51 KO ^{Mito}cpVenus and HEK293 SLC25A51 KO ^{Mito}Sensor cells using Lipofectamine 2000 (Invitrogen, 11668019) and relative steady state measurements were taken 48 h post-transfection using flow cytometry.

FlowJo was used to calculate the ratiometric measurement of the NAD⁺ biosensor and CpVenus control by dividing the fluorescence emission when excited at 488 nm with measurement when excited at 405 nm for each cell. The geometric mean of the ratiometric fluorescence measurement was taken for 10,000 cells for both NAD⁺ biosensor and CpVenus. This was used to calculate the relative fluorescence as follows:

$$(\text{Relative Fluorescence})^{-1} = \left(\frac{\text{Sensor}_{488}^{405}}{\text{CpVenus}_{488}^{405}} \right)^{-1}$$

Western blotting for overexpression studies

HeLa or HEK293 cells were lysed with 2× Laemmli sample buffer containing DTT. Lysates from 200,000 or 75,000 cells were resolved using NuPAGE™ 10% or 4–12% Bis-Tris protein gels (Invitrogen) and were transferred to Bio-Rad 0.45 µm nitrocellulose membrane. The nitrocellulose membrane was blocked with 5% BSA in pH 7.4 Tris-buffered saline with 0.1% (v/v) Tween 20 (TBST). The antibodies anti-Flag M2 (Sigma, F1804, 1:3,000), and anti-HSP60 Monoclonal Antibody (Invitrogen, 4B9/89, 1:3,000) were used for immunoblotting at 4°C overnight and were prepared in TBST with

1% BSA. After 3 washes of 5 min each, anti-Mouse IgG (H+L), Alexa Fluor™ Plus 800 (Invitrogen, A32730, 1:10,000) prepared in TBST with 1% BSA was hybridized for 1 h at room temperature. LiCOR Odyssey CLx was used for imaging after 3 washes with 1×TBST.

Western blotting for SLC25A51 knockout validation

HEK293 SLC25A51 knockout cells were washed with ice-cold PBS and lysed directly with 100 µl 2× Laemmli sample buffer containing DTT. 400,000 cells were electrophoresed on 10% Bis-Tris gels (Invitrogen) and transferred to 0.45 µm nitrocellulose membrane. Membranes were blocked with 5% nonfat milk in TBST at RT for 1 h. The primary antibody was prepared in 1% nonfat milk in TBST and hybridized at 4°C overnight. The secondary antibody was prepared in 1% nonfat milk in TBST and hybridized at room temperature for 1 h. Antibodies used and their dilutions are as follows: anti-SLC25A51 (MyBiosource, MBS1496255, 2 µg/ml), anti-HSP60 Monoclonal Antibody (Invitrogen, 4B9/89, 1:3,000), anti-rabbit IgG H&L IRDye 800CW (Abcam, ab216773, 1:10,000), and anti-mouse IgG H&L Alexa Fluor 680 (Invitrogen, A10038, 1:10,000). Membranes were imaged using the LiCOR Odyssey CLx.

Immunofluorescence

Cells were transfected with pCMV-Flag-HA-SLC25A51 (amino acids 1–297)-IRES-puro or the mutants and 24 h post-transfection were seeded on coverslips. At 48 h post-transfection, cells were washed and fixed in 500 µl using 4% PFA and 4% sucrose in PBS for 10 min at room temperature. Samples were washed three times with 1 ml of PBS followed by 10 min of blocking and permeabilization in solution containing: 5% Normal Goat Serum, 1% BSA, and 0.3% Triton-X 100 in PBS. After blocking, 50 µl of primary antibodies anti-flag D6W5B (Cell signaling, 14793) and anti-CoxIV Mouse (abcam ab33985) at 1:500 dilution in blocking solution were added on top of the coverslip for 1 h at room temperature. The coverslips were washed three times with 200 µl PBS and 50 µl of secondary antibodies were added onto the coverslips for 1 h at room temperature. This was followed by three times wash with PBS. Coverslips were mounted on slides using 5 µl VECTASHIELD Vibrance antifade mounting medium (NC1601054) and were allowed to set for 1 h at room temperature before imaging. Images were taken using an Olympus IX83 confocal microscope with an 100× objective and were analyzed using ImageJ.

Flag immunoprecipitation of ^{Flag}SLC25A51 and variants

HEK293T cells were transfected using PEI with wildtype ^{Flag}SLC25A51 and the variant with R82Q, R174Q, and R270Q mutations. Cells were harvested 2 days post-transfection, washed with ice-cold PBS and lysed with the lysis buffer containing 1% DDM, 20 mM Tris pH 8.0, 200 mM NaCl, and 2× Pierce™ Protease Inhibitor (A32965) for 1 h at 4°C. The lysates were centrifuged at 13,000 g at 4°C for 15 min. The supernatant was collected and incubated with Anti-DYKDDDDK affinity resin beads (Thermo Scientific Pierce, A36801) for 2 h at 4°C. After spinning down and removing the supernatant, the beads were washed three times using the lysis buffer. To elute the bound protein, 3× flag peptide (0.5 mg/ml) was added to the beads and incubated for 30 min at 4°C. The elution

steps were repeated a total of three times. Finally, the three eluates were combined for the cardiolipin binding assay.

Cardiolipin binding assay

Equivalent amounts of immunoprecipitated wildtype and mutant ^{Flag}SLC25A51 from HEK293T cells were incubated with 20 μl of cardiolipin-conjugated beads or control beads (Echelon Biosciences, P-BCLP) for 2 h at 4°C. Supernatant was removed and beads were washed three times in buffer containing 1% DDM, 20 mM Tris pH 8.0, 200 mM NaCl, and 2× Pierce™ Protease Inhibitor (A32965). 2× Laemmli sample buffer containing DTT was added to each sample of washed beads and analyzed by Western blotting using antibodies against anti-Flag M2 (Sigma, F1804, 1:3,000).

E. coli uptake assay

The protocol was adopted from a previously described uptake assay for ADP/ATP carrier (Haferkamp *et al.*, 2002). The pMW7 expression plasmids encoding YFP, SLC25A51 (amino acids 29–297) or its mutants were transformed into BL21 DE3 pLysS *E. coli* strain. The colonies were picked for each mutant and grown overnight. The overnight culture was diluted to 0.5 OD₆₀₀ and induced for 1 h with 1 mM IPTG. Cells equivalent to an OD₆₀₀ of 5 in a final reaction volume of 50 μl were aliquoted in tubes, spun down at 4,000 g for 5 min and resuspended in 25 μl of uptake buffer (120 mM KCl, 5 mM KH₂PO₄, 1 mM EGTA and 2 mM HEPES-NaOH pH 7.4). The reaction was started by adding 25 μl of uptake buffer with the final reaction concentration of 100 μM of unlabeled NAD⁺ traced with 3.33 nM of ³²P-NAD⁺. The reaction was stopped after 1 h by diluting it 20-fold with ice cold uptake buffer containing 200 μM NAD⁺. The reactions were spun down at 4,000 g for 5 min, the supernatant was discarded, and the cells were resuspended in 500 μl of uptake buffer (For uptake at different time points in Fig EV3E, this step was skipped). The samples were filtered through 0.22 μm mixed-cellulose ester filter using a filtration assembly with attached vacuum pump. The filter was washed two times with 5 and 3 ml uptake buffer. The filters were placed on a supporting sheet, wrapped with clingwrap and exposed to BioRad phosphorimaging screen in an exposure cassette for 18 h. Typhoon FLA 9500 Imager was used to image and ImageJ was used to quantify the dots. The intensity of the YFP control dot was subtracted for all the samples to account for non-specific binding or any non-active transport.

E. coli membrane enrichment and Western blot

The cultures were grown overnight and induced as described. Equivalent cells from the induced cultures for YFP, SLC25A51 (amino acids 29–297) and the mutants were spun down at 4,000 g for 5 min and washed with 1×PBS. The pellets were resuspended in 1 ml of 10 mM Tris/150 mM NaCl containing 1× Pierce™ Protease Inhibitor (A32965). Sonication was performed at 50% amplitude with 15 s ON/15 s OFF cycles for a total ON time of 5 min. The sonicated samples were spun down at 12,000 g for 30 min at 4°C. Supernatant was ultracentrifuged to pellet the membrane fraction at 100,000 g for 45 min at 4°C. The membrane pellet was resuspended in 100 μl of 50 mM Tris/150 mM NaCl with 1× protease inhibitor. 2× Laemmli sample buffer containing DTT was added to each

sample and the samples were resolved with NuPAGE™ 10% Bis-Tris protein gels (Invitrogen), transferred to Bio-Rad 0.45 μm nitrocellulose membrane and blocked with 5% BSA in TBST. Immunoblotting was done using the following antibodies at 4°C overnight: anti-SLC25A51 (Prosci-Inc, 55-424, 1:500), anti-TolC (Mavridou lab at UT Austin, 1:2,000) and anti-DNAK *E. coli* (Enzo ADI-SPA-880-D, 1:5,000). After 3 washes in 1× TBST, the anti-Mouse IgG (H+L), Alexa Fluor™ Plus 800 (Invitrogen, A32730, 1:10,000) or anti-Rabbit IgG (H+L), Alexa Fluor™ 680 (Invitrogen, A27042, 1:10,000) was hybridized for 1 h at room temperature. This was followed by 3 wash steps in 1× TBST and imaging using LiCOR Odyssey CLx.

Statistical analysis and figure graphics

The results are presented as mean ± SD in box and whisker graphical format. The data was analyzed, and figures were prepared using GraphPad Prism version 9, Microsoft Excel, and adobe illustrator. *P*-values were determined using unpaired two-sided *t*-test (for two group comparison) and one-way ANOVA (for 3 or more group comparisons) with post-hoc Dunnett's test. *P*-values under 0.05 were considered significant and **P* < 0.05, ***P* < 0.01 and ****P* < 0.001.

Data availability

Full view images, all data points, and simulation models are available via the Texas Data Repository, Cambronne XA Lab Dataverse <https://doi.org/10.18738/T8/TIHMRO>.

Expanded View for this article is available [online](#).

Acknowledgements

We thank Dr. Ron Elber and Dr. Liao Chen for valuable discussions. We also thank Dr. Despoina Mavridou for providing us with the TolC antibody and Dr. Gennaro Agrimi for the pMW7 plasmid. Supported by the Texas Advanced Computing Center, NIH DP2 GM126897, the Pew Charitable Trust, and CPRIT RP210079.

Author contributions

Shivansh Goyal: Conceptualization; data curation; software; formal analysis; investigation; writing – original draft; writing – review and editing. **Akhilesh Paspureddi:** Software; formal analysis. **Mu-Jie Lu:** Investigation; writing – review and editing. **Hsin-Ru Chan:** Investigation; writing – review and editing. **Scott N Lyons:** Investigation; writing – review and editing. **Crystal N Wilson:** Validation. **Marc Niere:** Resources; writing – review and editing. **Mathias Ziegler:** Resources; writing – review and editing. **Xiaolu A Cambronne:** Conceptualization; supervision; funding acquisition; writing – original draft; project administration; writing – review and editing.

Disclosure and competing interests statement

The authors declare that they have no conflict of interest.

References

- Abraham MJ, Murtola T, Schulz R, Páll S, Smith JC, Hess B, Lindahl E (2015) GROMACS: high performance molecular simulations through multi-level parallelism from laptops to supercomputers. *SoftwareX* 1–2: 19–25

- Bekker H, Berendsen HJC, Dijkstra EJ, Achterop S, Vondrumen R, Vanderspoel D, Sijbers A, Keegstra H, Renardus MKR (1993) Gromacs: a parallel computer for molecular dynamics simulations. In *Physics Computing 92*, de Groot RA, Nadrchal J (eds), pp 252–256. Singapore: World Scientific
- Cambronne XA, Stewart ML, Kim D, Jones-Brunette AM, Morgan RK, Farrens DL, Cohen MS, Goodman RH (2016) Biosensor reveals multiple sources for mitochondrial NAD⁺. *Science* 352: 1474–1477
- Cimadamore-Werthein C, Baron SJ, King MS, Springett R, Kunji ER (2023) Human mitochondrial ADP/ATP carrier SLC25A4 operates with a ping-pong kinetic mechanism. *EMBO Rep* 24: e57127
- Comte J, Ma sterrena B, Gautheron DC (1976) Lipid composition and protein profiles of outer and inner membranes from pig heart mitochondria. Comparison with microsomes. *Biochim Biophys Acta* 419: 271–284
- Crichton PG, Lee Y, Ruprecht JJ, Cerson E, Thangaratnarajah C, King MS, Kunji ERS (2015) Trends in thermostability provide information on the nature of substrate, inhibitor, and lipid interactions with mitochondrial carriers. *J Biol Chem* 290: 8206–8217
- Dehez F, Pebay-Peyroula E, Chipot C (2008) Binding of ADP in the mitochondrial ADP/ATP carrier is driven by an electrostatic funnel. *J Am Chem Soc* 130: 12725–12733
- Dowhan W (1997) Molecular basis for membrane phospholipid diversity: why are there so many lipids? *Annu Rev Biochem* 66: 199–232
- Duncan AL, Ruprecht JJ, Kunji ERS, Robinson AJ (2018) Cardiolipin dynamics and binding to conserved residues in the mitochondrial ADP/ATP carrier. *Biochim Biophys Acta Biomembr* 1860: 1035–1045
- Eller JM, Stewart ML, Slepian AJ, Markwardt S, Wiedrick J, Cohen MS, Goodman RH, Cambronne XA (2019) Flow cytometry analysis of free intracellular NAD⁺ using a targeted biosensor. *Curr Protoc Cytom* 88: 1–27
- Eller J, Goyal S, Cambronne XA (2023) Improved yield for the enzymatic synthesis of radiolabeled nicotinamide adenine dinucleotide. *ACS Bio Med Chem Au* 3: 46–50
- Forli S, Huey R, Pique ME, Sanner MF, Goodsell DS, Olson AJ (2016) Computational protein–ligand docking and virtual drug screening with the AutoDock suite. *Nat Protoc* 11: 905–919
- Girardi E, Agrimi G, Goldmann U, Fiume G, Lindinger S, Sedlyarov V, Srdic I, Gürtl B, Agerer B, Kartnig F et al (2020) Epistasis-driven identification of SLC25A51 as a regulator of human mitochondrial NAD import. *Nat Commun* 11: 6145
- Haferkamp I, Hackstein JHP, Voncken FGJ, Schmit G, Tjaden J (2002) Functional integration of mitochondrial and hydrogenosomal ADP/ATP carriers in the *Escherichia coli* membrane reveals different biochemical characteristics for plants, mammals and anaerobic chytrids. *Eur J Biochem* 269: 3172–3181
- Heidkämper D, Müller V, Nelson DR, Klingenberg M (1996) Probing the role of positive residues in the ADP/ATP carrier from yeast. The effect of six arginine mutations on transport and the four ATP versus ADP exchange modes. *Biochemistry* 35: 16144–16152
- Hung YP, Albeck JG, Tantama M, Yellen G (2011) Imaging cytosolic NADH–NAD⁺ redox state with a genetically encoded fluorescent biosensor. *Cell Metab* 14: 545–554
- Jo S, Kim T, Im W (2007) Automated builder and database of protein/membrane complexes for molecular dynamics simulations. *PLoS One* 2: e880
- Jo S, Kim T, Iyer VG, Im W (2008) CHARMM-GUI: a web-based graphical user interface for CHARMM. *J Comput Chem* 29: 1859–1865
- Jones SA, Gogoi P, Ruprecht JJ, King MS, Lee Y, Zögg T, Pardon E, Chand D, Steimle S, Copeman DM et al (2023) Structural basis of purine nucleotide inhibition of human uncoupling protein 1. *Sci Adv* 9: eadh4251
- Jumper J, Evans R, Pritzel A, Green T, Figurnov M, Ronneberger O, Tunyasuvunakool K, Bates R, Židek A, Potapenko A et al (2021) Highly accurate protein structure prediction with AlphaFold. *Nature* 596: 583–589
- Kang Y, Chen L (2023) Structural basis for the binding of DNP and purine nucleotides onto UCP1. *Nature* 620: 226–231
- King MS, Kerr M, Crichton PG, Springett R, Kunji ERS (2016) Formation of a cytoplasmic salt bridge network in the matrix state is a fundamental step in the transport mechanism of the mitochondrial ADP/ATP carrier. *Biochim Biophys Acta Bioenerg* 1857: 14–22
- Kory N, de Bos J u, van der Rijt S, Jankovic N, Gura M, Arp N, Pena IA, Prakash G, Chan SH, Kunchok T et al (2020) MCART1/SLC25A51 is required for mitochondrial NAD transport. *Sci Adv* 6: eabe5310
- Krammer EM, Ravaud S, Dehez F, Frelet-Barrand A, Pebay-Peyroula E, Chipot C (2009) High-chloride concentrations abolish the binding of adenine nucleotides in the mitochondrial ADP/ATP carrier family. *Biophys J* 97: L25–L27
- Kunji ERS, Robinson AJ (2006) The conserved substrate binding site of mitochondrial carriers. *Biochim Biophys Acta Bioenerg* 1757: 1237–1248
- Lee J, Cheng X, Swails JM, Yeom MS, Eastman PK, Lemkul JA, Wei S, Buckner J, Jeong JC, Qi Y et al (2016) CHARMM-GUI input generator for NAMD, GROMACS, AMBER, OpenMM, and CHARMM/OpenMM simulations using the CHARMM36 additive force field. *J Chem Theory Comput* 12: 405–413
- Luongo TS, Eller JM, Lu MJ, Niere M, Raith F, Perry C, Bornstein MR, Oliphint P, Wang L, McReynolds MR et al (2020) SLC25A51 is a mammalian mitochondrial NAD⁺ transporter. *Nature* 588: 174–179
- Majd H, King MS, Palmer SM, Smith AC, Elbourne LDH, Paulsen IT, Sharples D, Henderson PJF, Kunji ERS (2018) Screening of candidate substrates and coupling ions of transporters by thermostability shift assays. *Elife* 7: 1–17
- Mao X, Yao S, Yi Q, Xu ZM, Cang X (2021) Function-related asymmetry of the specific cardiolipin binding sites on the mitochondrial ADP/ATP carrier. *Biochim Biophys Acta Biomembr* 1863: 183466
- Mavridou V, King MS, Tavoulari S, Ruprecht JJ, Palmer SM, Kunji ERS (2022) Substrate binding in the mitochondrial ADP/ATP carrier is a step-wise process guiding the structural changes in the transport cycle. *Nat Commun* 13: 1–12
- Mejia EM, Hatch GM (2015) Mitochondrial phospholipids: role in mitochondrial function. *J Bioenerg Biomembr* 482: 99–112
- Mifsud J, Ravaud S, Krammer EM, Chipot C, Kunji ERS, Pebay-Peyroula E, Dehez F (2013) The substrate specificity of the human ADP/ATP carrier AAC1. *Mol Membr Biol* 30: 160–168
- Miniero DV, Monné M, Di Noia MA, Palmieri L, Palmieri F (2022) Evidence for non-essential salt bridges in the M-gates of mitochondrial carrier proteins. *Int J Mol Sci* 23: 5060
- Monné M, Palmieri F, Kunji ERS (2013) The substrate specificity of mitochondrial carriers: mutagenesis revisited. *Mol Membr Biol* 30: 149–159
- Morris GM, Ruth H, Lindstrom W, Sanner MF, Belew RK, Goodsell DS, Olson AJ (2009) Software news and updates AutoDock4 and AutoDockTools4: automated docking with selective receptor flexibility. *J Comput Chem* 30: 2785–2791
- Nelson DR, Felix CM, Swanson JM (1998) Highly conserved charge-pair networks in the mitochondrial carrier family. *J Mol Biol* 277: 285–308
- Nury H, Dahout-Gonzalez C, Trézéguet V, Lauquin G, Brandolin G, Pebay-Peyroula E (2005) Structural basis for lipid-mediated interactions between mitochondrial ADP/ATP carrier monomers. *FEBS Lett* 579: 6031–6036
- Okonechnikov K, Golosova O, Fursov M, Varlamov A, Vaskin Y, Efremov I, German Grehov OG, Kandrov D, Rasputin K, Syabro M et al (2012) Unipro UGENE: a unified bioinformatics toolkit. *Bioinformatics* 28: 1166–1167
- Olofsson G, Sparr E (2013) Ionization constants pKa of cardiolipin. *PLoS One* 8: e73040

- Omasits U, Ahrens CH, Müller S, Wollscheid B (2014) Protter: interactive protein feature visualization and integration with experimental proteomic data. *Bioinformatics* 30: 884–886
- Palmieri F (2013) The mitochondrial transporter family SLC25: identification, properties and physiopathology. *Mol Aspects Med* 34: 465–484
- Palmieri F, Rieder B, Ventrella A, Blanco E, Do PT, Nunes-Nesi A, Trauth AU, Fiermonte G, Tjaden J, Agrimi G et al (2009) Molecular identification and functional characterization of *Arabidopsis thaliana* mitochondrial and chloroplastic NAD⁺ carrier proteins. *J Biol Chem* 284: 31249–31259
- Papadopoulos JS, Agarwala R (2007) COBALT: constraint-based alignment tool for multiple protein sequences. *Bioinformatics* 23: 1073–1079
- Pebay-Peyroula E, Dahout-Gonzalez C, Kahn R, Trézéguet V, Lauquin GJM, Brandolin G (2003) Structure of mitochondrial ADP/ATP carrier in complex with carboxyatractyloside. *Nature* 426: 39–44
- Pierrri CL, Palmieri F, De Grassi A (2014) Single-nucleotide evolution quantifies the importance of each site along the structure of mitochondrial carriers. *Cell Mol Life Sci* 71: 349–364
- Ran FA, Hsu PD, Wright J, Agarwala V, Scott DA, Zhang F (2013) Genome engineering using the CRISPR-Cas9 system. *Nat Protoc* 8: 2281–2308
- Ravaud S, Bidon-Chanal A, Blesneac I, MacHillot P, Juillan-Binard C, Dehez F, Chipot C, Pebay-Peyroula E (2012) Impaired transport of nucleotides in a mitochondrial carrier explains severe human genetic diseases. *ACS Chem Biol* 7: 1164–1169
- Robinson AJ, Kunji ERS (2006) Mitochondrial carriers in the cytoplasmic state have a common substrate binding site. *Proc Natl Acad Sci USA* 103: 2617–2622
- Robinson AJ, Overy C, Kunji ERS (2008) The mechanism of transport by mitochondrial carriers based on analysis of symmetry. *Proc Natl Acad Sci USA* 105: 17766–17771
- Ruprecht JJ, Kunji ERS (2021) Structural mechanism of transport of mitochondrial carriers. *Annu Rev Biochem* 90: 535–558
- Ruprecht JJ, Hellawell AM, Harding M, Crichton PG, McCoy AJ, Kunji ERS (2014) Structures of yeast mitochondrial ADP/ATP carriers support a domain-based alternating-access transport mechanism. *Proc Natl Acad Sci USA* 111: E426–E434
- Ruprecht JJ, King MS, Zögg T, Aleksandrova AA, Pardon E, Crichton PG, Steyaert J, Kunji ERS (2019) The molecular mechanism of transport by the mitochondrial ADP/ATP carrier. *Cell* 176: 435–447
- Sathappa M, Alder NN (2016) The ionization properties of cardiolipin and its variants in model bilayers. *Biochim Biophys Acta Biomembr* 1858: 1362–1372
- Senoo N, Kandasamy S, Ogunbona OB, Baile MG, Lu Y, Claypool SM (2020) Cardiolipin, conformation, and respiratory complex-dependent oligomerization of the major mitochondrial ADP/ATP carrier in yeast. *Sci Adv* 6: 780–808
- Senoo N, Chinthapalli DK, Baile MG, Golla VK, Saha B, Ogunbona OB, Saba JA, Munteanu T, Valdez Y, Whited K et al (2023) Conserved cardiolipin-mitochondrial ADP/ATP carrier interactions assume distinct structural and functional roles that are clinically relevant. *bioRxiv* <https://doi.org/10.1101/2023.05.05.539595> [PREPRINT]
- Springett R, King MS, Crichton PG, Kunji ERS (2017) Modelling the free energy profile of the mitochondrial ADP/ATP carrier. *Biochim Biophys Acta Bioenerg* 1858: 906–914
- Studer G, Rempfer C, Waterhouse AM, Gumienny R, Haas J, Schwede T (2020) QMEANDisCo-distance constraints applied on model quality estimation. *Bioinformatics* 36: 1765–1771
- Todisco S, Agrimi G, Castegna A, Palmieri F (2006) Identification of the mitochondrial NAD⁺ transporter in *Saccharomyces cerevisiae*. *J Biol Chem* 281: 1524–1531
- Tomasello G, Armenia I, Molla G (2020) The Protein Imager: a full-featured online molecular viewer interface with server-side HQ-rendering capabilities. *Bioinformatics* 36: 2909–2911
- Wang Y, Tajkhorshid E (2008) Electrostatic funneling of substrate in mitochondrial inner membrane carriers. *Proc Natl Acad Sci USA* 105: 9598–9603
- Waterhouse A, Bertoni M, Bienert S, Studer G, Tauriello G, Gumienny R, Heer FT, De Beer TAP, Rempfer C, Bordoli L et al (2018) SWISS-MODEL: homology modelling of protein structures and complexes. *Nucleic Acids Res* 46: W296–W303
- Williams CJ, Headd JJ, Moriarty NW, Prisant MG, Videau LL, Deis LN, Verma V, Keedy DA, Hintze BJ, Chen VB et al (2018) MolProbity: more and better reference data for improved all-atom structure validation. *Protein Sci* 27: 293–315
- Williamson DH, Lund P, Krebs HA (1967) The redox state of free nicotinamide-adenine dinucleotide in the cytoplasm and mitochondria of rat liver. *Biochem J* 103: 514–527
- Wu EL, Cheng X, Jo S, Rui H, Song KC, Dávila-Contreras EM, Qi Y, Lee J, Monje-Galvan V, Venable RM et al (2014) CHARMM-GUI membrane builder toward realistic biological membrane simulations. *J Comput Chem* 35: 1997–2004
- Yi Q, Li Q, Yao S, Chen Y, Guan MX, Cang X (2019) Molecular dynamics simulations on apo ADP/ATP carrier shed new lights on the featured motif of the mitochondrial carriers. *Mitochondrion* 47: 94–102
- Yi Q, Yao S, Ma B, Cang X (2022) The effects of cardiolipin on the structural dynamics of the mitochondrial ADP/ATP carrier in its cytosol-open state. *J Lipid Res* 63: 100227
- Zhang Q, Piston DW, Goodman RH (2002) Regulation of corepressor function by nuclear NADH. *Science* 295: 1895–1897
- Zhao Y, Jin J, Hu Q, Zhou HM, Yi J, Yu Z, Xu L, Wang X, Yang Y, Loscalzo J (2011) Genetically encoded fluorescent sensors for intracellular NADH detection. *Cell Metab* 14: 555–566
- Ziegler M, Monné M, Nikiforov A, Agrimi G, Heiland I, Palmieri F (2021) Welcome to the family: identification of the NAD⁺ transporter of animal mitochondria as member of the solute carrier family SLC25. *Biomolecules* 11: 880